# High-entropy carbons: From high-entropy aromatic species to single-atom catalysts for electrocatalysis

Ding, J.; Wu, D.; Zhu, J.; Rodríguez-Hernández, F.; Chen, Y.; Lu, C.; Zhou, S.; Zhang, J.; Tranca, D.; Zhuang, X.;

Originally published:

July 2021

**Chemical Engineering Journal 426(2021), 131320**

DOI: https://doi.org/10.1016/j.cej.2021.131320

# High-Entropy Carbons: from High-Entropy Aromatic Species to Single-Atom Catalysts for Electrocatalysis

*Junjie Ding,[a,b] Dongchuang Wu,[a,b] Jinhui Zhu,[b] Senhe Huang,[b] Fermín Rodríguez-Hernández,[c] Yu Chen,*[a] Chenbao Lu,[b,e] Shengqiang Zhou,[d] Jichao Zhang,*[f] Diana Tranca,*[b] Xiaodong Zhuang*[b]*

[a] Key Lab for Advanced Materials, Institute of Applied Chemistry, East China University of Science and Technology,130 Meilong Road, Shanghai 200237, China.

[b] The meso-Entropy Matter Lab, State Key Laboratory of Metal Matrix Composites, Shanghai Key Laboratory of Electrical Insulation and Thermal Ageing, School of Chemistry and Chemical Engineering, Shanghai Jiao Tong University, 800 Dongchuan Road, Shanghai 200240, China.

[c] Max Planck Institute for the Physics of Complex Systems, Nöthnitzer Str. 38, Dresden 01187, Germany.

[d] Helmholtz-Zentrum Dresden-Rossendorf, Institute of Ion Beam Physics and Materials Research, Bautzner Landstr. 400, 01328 Dresden, Germany.

[e] College of Chemistry and Molecular Engineering, Zhengzhou University. 100 Science Avenue, Zhengzhou 450001, Henan, China.

[f] Shanghai Synchrotron Radiation Facility, Zhangjiang Laboratory, Shanghai Advanced Research Institute, Chinese Academy of Sciences, No. 239, Zhangheng Road, Shanghai 201204, China.

**Corresponding Author**

Yu Chen: E-mail: chentangyu@yahoo.com

Jichao Zhang: E-mail: zhangjichao@zjlab.org.cn

Diana Tranca: E-mail: diana.tranca@sjtu.edu.cn

Xiaodong Zhuang: E-mail: zhuang@sjtu.edu.cn

**Abstract**

Single-atom catalysts (SACs) have rapidly entered the field of nanomaterials and demonstrated great potential for energy devices in recent years. Of all types of SACs, porous carbon-based SACs are the most popular species because of their excellent conductivity, large specific surface area, and easily tunable heteroatom and metal components. However, most of the reported cases focus on the metal centers and their coordination environments, while they do not pay much attention to carbon precursors and carbon transformation during high-temperature treatment. In this work, we use a high-entropy aromatic molecule, azulene, for rational synthesis of azulene-enriched, sandwich-like polymer nanosheets and corresponding single-Fe-dispersed porous carbon nanosheets. The azulene-based metal-free polymer nanosheets exhibit a narrow band gap and temperature-dependent magnetism. As proof-of-concept electrocatalysts for $CO_2$ reduction, the prepared carbon nanosheets exhibit high activity and stability. Operando X-ray absorption spectroscopy and density functional theory studies reveal the high activity of Fe-N coordination sites in the presence of 5/7-membered carbon ring-based topological defects in the carbon skeleton. Taken together, this work provides a new method of synthesizing high-entropy carbons using azulene-based high-entropy molecule as precursor and paves the way toward high-efficiency SACs with rich topological defects for energy conversion.

**Keywords**: high-entropy aromatic molecule, topological defect, single-atom catalyst, porous carbon nanosheet, carbon dioxide conversion

## 1. Introduction

Environmental pollution and energy shortage have become serious problems for human beings and are required to be addressed urgently. Massive consumption of fossil fuels has sharply increased the emission of carbon dioxide ($CO_2$). To overcome this issue, electrochemical reduction of $CO_2$ into valuable chemicals, such as carbon monoxide, formic acid, and methane, has been considered as an effective method of easing the energy crisis and reducing the greenhouse effect [1-5]. However, designing effective electrocatalysts for $CO_2$ reduction reaction ($CO_2$RR) with a high activity, selectivity and stability remains challenging because of the high C=O bond energy (803 KJ $mol^{-1}$) and competing hydrogen evolution reaction (HER) [6-8]. In order to improve the conversion efficiency, a broad range of $CO_2$RR catalysts have been reported, including metal or metal alloys [9,10], immobilized N-C complexes [11,12], single-transition metal atom-dispersed carbons [13-16], metal organic frameworks [17,18], and metal-free heteroatom-doped carbon nanomaterials [19-21]. Among these materials, both single-atom-dispersed and heteroatom-doped carbons have been regarded as the most promising candidates for $CO_2$RR because of their high conductivity, large specific surface area, easily tunable heteroatom and metal components, and available carbon precursors [22-24]. Single-atom catalysts (SACs) have attracted great interest in recent years because of their excellent catalytic performance, and they are easy experimental materials for studies on atomic-level understanding of the structure–property relationship in the catalysis field [25-29]. Compared with traditional heterogeneous catalysts, SACs can maximize atomic utilization and further enhance catalytic activity and selectivity [30,31]. Although SACs exhibit great potential in the electrocatalytic field, their rational preparation is arduous because of their tendency to aggregate into clusters and nanoparticles at high temperatures. Therefore, different carbon precursors were used to prepare SACs for $CO_2$RR to achieve high stability of

atomically dispersed metal sites. However, most of them did not have typical advantages because of the uncontrollable pyrolysis process [32].

High specific surface areas of porous carbons can guarantee efficient accessibility of active sites during catalysis. The high specific surface areas of porous carbons originate mainly from topological defects (non-six-membered carbon rings compared with benzene-unit-dominated graphite) which have long been ignored by the community [33-37]. A few studies have reported that structures with topological defects can act as active sites for $CO_2$RR [38]. Furthermore, Siahrostami et al. used theoretical calculation and predicted positive $CO_2$RR performance for a series of carbons with topological defects [39]. These results indicated that N-doped carbons with pentagon and heptagon rings exhibited high activity comparable with that of pyridinic-N for $CO_2$RR. Although such studies are extremely limited, they inspired us to develop porous carbons with rich topological defects for $CO_2$RR. So far, physical methods, e.g., electron/ion beam irradiation, laser scribing, and arc-discharging, have been developed for fabricating topological defects in graphene, carbon nanotube, and other carbon materials [33,40-44]. However, these physical methods can only be used for localized areas and cannot be used for large-scale preparation.

In this study, we developed an effective strategy to synthesize atomically Fe-dispersed porous carbon nanosheets with topological defects using high-entropy azulene-dominated material as a precursor. Azulene has been proven to be the high-entropy isomer of naphthalene (Fig. S1) [44,45]. The presence of azulene units in a carbon skeleton could promote the formation of single atom catalysts. Azulene, with 5/7-membered carbon rings and intrinsic polarity, was used as building block to fabricate graphene-coupled, sandwich-like polymer nanosheets. Upon undergoing iron cation anchoring and pyrolysis, Fe/N co-doped porous carbon nanosheets with topological defects

can be easily prepared on a large scale. As electrocatalysts for $CO_2RR$, as-prepared catalysts exhibited promising $CO_2RR$ catalytic activity with a maximum Faradic efficiency of CO ($FE_{CO}$) of 95.3% in 0.5 M $KHCO_3$, surpassing most reported Fe-based catalysts. Operando X-ray absorption spectroscopy and density functional theory (DFT) studies were performed to further understand the relationship between active sites and high $CO_2RR$ performance. This study offers a new method of rational preparation of porous carbons with both single metal atoms and several topological defects for electrocatalytic $CO_2RR$.

## 2. Experimental section

### *2.1 Preparation of GPAz*

Poly(2-aminoazulene) functionalized graphene oxide nanosheets were prepared by direct polymerization of 2-aminoazulene on GO in aqueous solution. Firstly, GO (66 mg) and ammonium persulfate (3 g, 13.1 mmol) were transferred into a 2 L round-bottomed flask and deionized water (1 L) was then added to dissolve them. Followed by ultrasonication for 30 min, a homogeneous suspension formed. Then, 2-aminoazulene (1 g, 7.0 mmol), dissolved in 1 M HCl (250 mL), was added to above GO solution and vigorously stirred overnight. Then, the resulting gray suspension was filtrated and washed with deionized water for three times to obtain polyaminoazulene covered GO (denoted as GPAz). GPNA was synthesized as a control sample by the same procedure using 2-naphthylamine as monomer instead of 2-aminoazulene. PAz and PNA were synthesized by the same procedure using 2-aminoazulene and 2-naphthylamine as monomers without GO.

### *2.2 Preparation of Fe@PCN-T*

Typically, $FeCl_3$ (100 mg 0.62 mmol) was dissolved in 30 mL deionized water and then missed with GPAz (200 mg). The mixture was vigorously stirred overnight. Subsequently, the solvent of the mixture was removed by reduced pressure to deliver fine powder. Then such powder

was carbonized at 800-1000 ℃ under Ar atmosphere for 2 h at the heating rate of 5 ℃ $min^{-1}$ to obtained Fe/N-doped porous carbon nanosheets (denoted as Fe@PCN-T, T=800-1000). Similarly, Fe/N-doped porous carbons (denoted as Fe@PCN'-T and Fe@PC-T, T=800-1000) were fabricated by using Fe ion absorbed GPNA and PAz as the starting material. In addition, metal-free porous carbon nanosheets (denoted as PCN-T, T=800-1000) were also prepared by using GPAz and GPNA as the starting materials, respectively. Furthermore, in order to activate the samples, PCN-T, Fe@PCN-T, Fe@PCN'-T and Fe@PC-T were further treated in $NH_3$ atmosphere at 800-1000 ℃ for 20 min to produce activated samples, which were denoted as PCN-Ta, Fe@PCN-Ta, Fe@PCN'-Ta and Fe@PC-Ta, T=800-1000).

**3. Results and discussion**

The procedure of synthesizing azulene-containing, sandwich-like polymer nanosheets is illustrated in Scheme 1. First, graphene oxide (GO) and ammonium persulfate were dissolved in deionized water. Next, protonated 2-aminoazulene was added and polymerized on the GO surface to produce azulene-containing, sandwich-like poly(2-aminoazulene) nanosheets (GPAz). The control experiment was also performed in the same procedure but without using GO to produce poly(2-aminoazulene) without two-dimensional (2D) morphology (denoted as PAz) and using 2-naphthylamine, the isomeride of 2-aminoazulene, as monomer to prepare sandwich-like benzene-dominated polymer nanosheets (denoted as GPNA, Fig. S2). This procedure provides a new method to prepare azulene-based 2D soft nanomaterials. The easy availability of the monomer and conventional oxidation polymerization method guarantee a large-scale preparation.

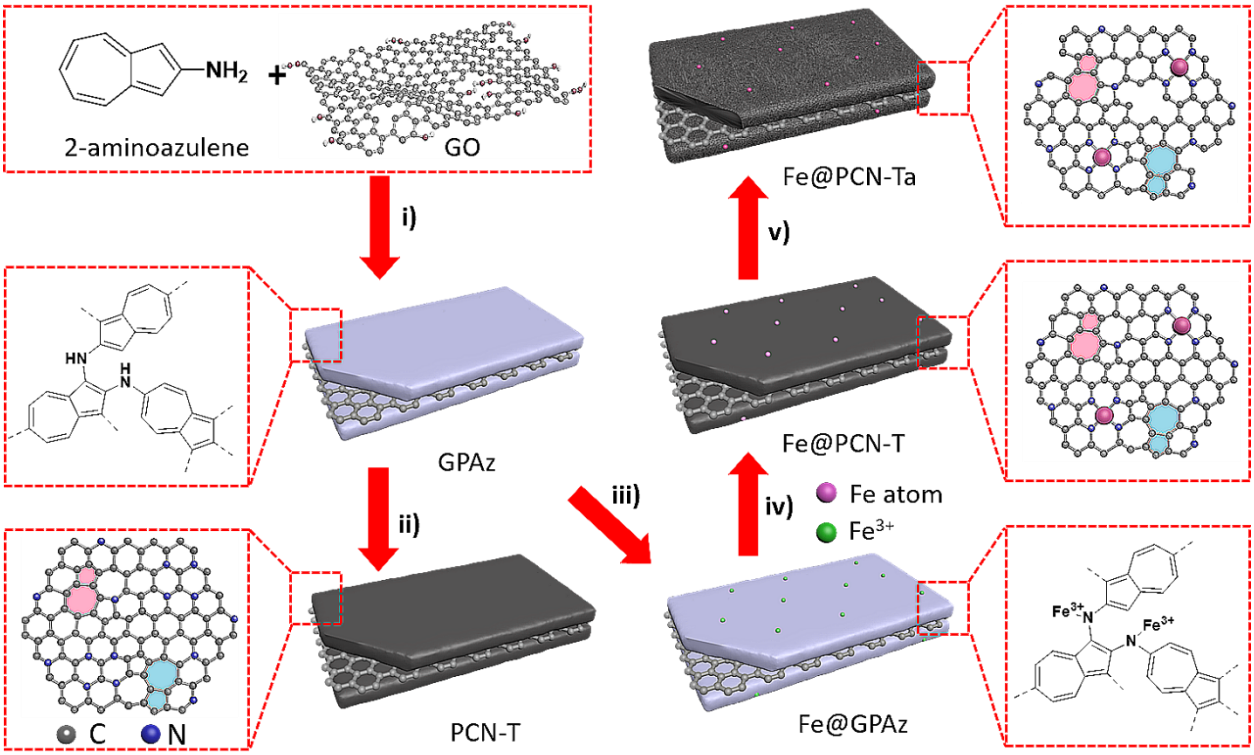


**Scheme 1.** Synthesis of azulene-based sandwich-like polymer nanosheets and single-Fe-dispersed porous carbon nanosheets. (i) HCl, ammonium persulfate, rt, 4 h. (ii) Ar, 600–1000 °C, 2 h. (iii) dispersing in $FeCl_3$ solution, 1 h. (iv) Ar, 800–1000 °C, 2 h. (v) ammonia activation at 800–1000°C for 20 min, followed by etching by HCl solution.

The morphology of as-prepared GPAz was characterized through scanning electron microscopy (SEM), transmission electron microscopy (TEM) and atomic force microscopy (AFM). As shown in Fig. 1a and Fig. S3a, GPAz demonstrates a uniform sheet-like structure. No free PAz particles (Fig. S3b) and naked GO nanosheets are observed, suggesting that almost all of the 2-aminoazulene was polymerized on the surface of GO. The TEM image (Fig. 1b) further illustrates the 2D sheet-like morphology of GPAz. To evaluate the loading capacity of GO, different weight ratios (1:5, 1:10, 1:15 and 1:20) of GO to 2-aminoazulene were used to fabricate

GPAz (1:5), GPAz (1:10), GPAz (1:15), and GPAz (1:20), respectively. As shown in Fig. 1c and Fig. S4, the thicknesses of GPAz (1:5), GPAz (1:10), GPAz (1:15) and GPAz (1:20) are 12 ± 5, 22 ± 5, 30 ± 4, and 40 ± 5 nm, respectively. This result indicates that by using GO as the template, we could not only easily obtain the uniform sheet-like structure in large quantities but also control the thickness by adjusting the weight ratio of GO to 2-aminoazulene.

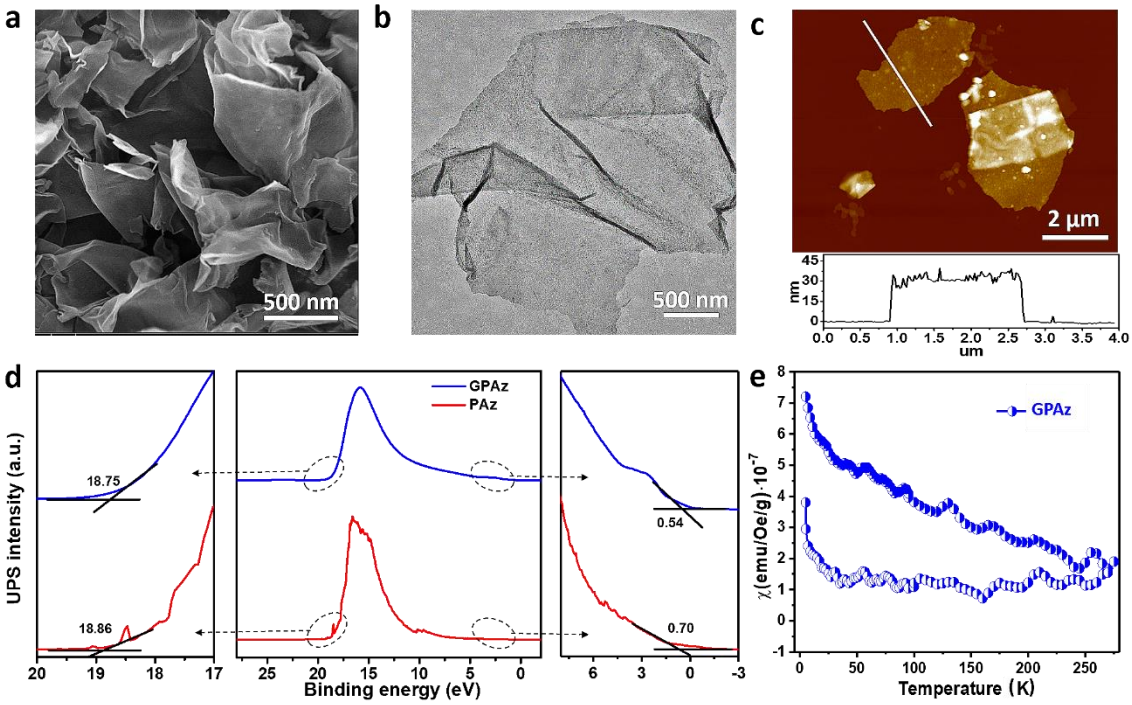


**Fig. 1.** Morphology and intrinsic properties of GPAz. (a) SEM, (b) TEM and (c) AFM images of GPAz. (d) UPS spectra of GPAz and PAz. (e) ZFC and FC curves of GPAz under the applied dc magnetic field of 100 Oe.

Ultraviolet photoelectron spectroscopy (UPS) could be used to determine the energy level of the highest occupied molecular orbital (HOMO) of semiconductive materials by subtracting the UPS width from excitation energy (HeI, 21.22 eV) [46]. According to Fig. 1d, the HOMO levels of GPAz and PAz are determined as −3.01 and −3.06 eV, respectively. According to the onset reduction and oxidation potentials of the cyclic voltammetry (CV) curves (Fig. S5), the energy

bandgaps ($E_g$) of GPAz and PAz can be further estimated as 0.95 and 0.92 eV, respectively. Therefore, the lowest unoccupied molecular orbital of GPAz and PAz were calculated as −2.06 and −2.14 eV, respectively, from HOMO + $E_g$. Such narrow bandgaps offer great opportunities for GPAz- and PAz-based optoelectronic devices. Azulene-enriched conjugated structures easily generate free radicals [47,48]. Therefore, electron paramagnetic resonance (EPR) were used to detect unpaired electrons or free radicals. The EPR spectra (Fig. S6) exhibits similar EPR signals (g = 2.0040) for both GPAz and PAz, indicating the existence of free radicals in both materials. Temperature-dependent magnetism was confirmed by zero-field-cooled (ZFC) and field-cooled (FC) measurements. The FC curve for GPAz shows a decrease with increasing temperature (Fig. 1e). A clear signature of magnetic ordering appears at approximately 270 K, which can be attributed to the rich free radicals from the azulene structure. At temperatures < 270 K, the FC and ZFC curves diverge. From the temperature-dependent remnant magnetism curve at H = 0 in Fig. S7, the remnant magnetism does not decrease to zero even at 270 K, which is consistent with the ZFC and FC results. All these results indicate that GPAz possesses unique optoelectronic and magnetic features, and could be used as a key component of semiconductor devices.

After pyrolysis of GPAz at 600–1000 °C in Ar atmosphere, N-doped porous carbon nanosheets (PCN-T, T = 600, 800, and 1000) were easily prepared. The TGA curve of GPAz (Fig. S8) shows a weight loss of 28% at 800 °C, whereas the weight loss of PAz reaches 55%, indicating the better thermal stability of GPAz nanosheets. All PCNs maintained the sheet-like morphology after pyrolysis (Fig. S9). GO not only serves as a template to control the 2D morphology, but also increases the long-distance conductivity of the carbon nanosheet after pyrolysis, which could be beneficial for electrocatalysis. The porosity of GPAz and PCN-T was then tested using $N_2$ sorption measurement. The Brunauer–Emmett–Teller specific surface areas of GPAz, PCN-600, PCN-800,

and PCN-1000 were calculated to be 256, 591, 735, and 720 $m^2 g^{-1}$, respectively (Fig. S10). From the pore size distributions (Fig. S11), all samples exhibit both micropores (<2 nm) and mesopores (2–50 nm). The $N_2$ sorption results of as-prepared samples were summarized in Table S1. These results indicate that the approach could be a new method of preparing porous carbons with intrinsic large specific surface areas without using any pore-creating templates.

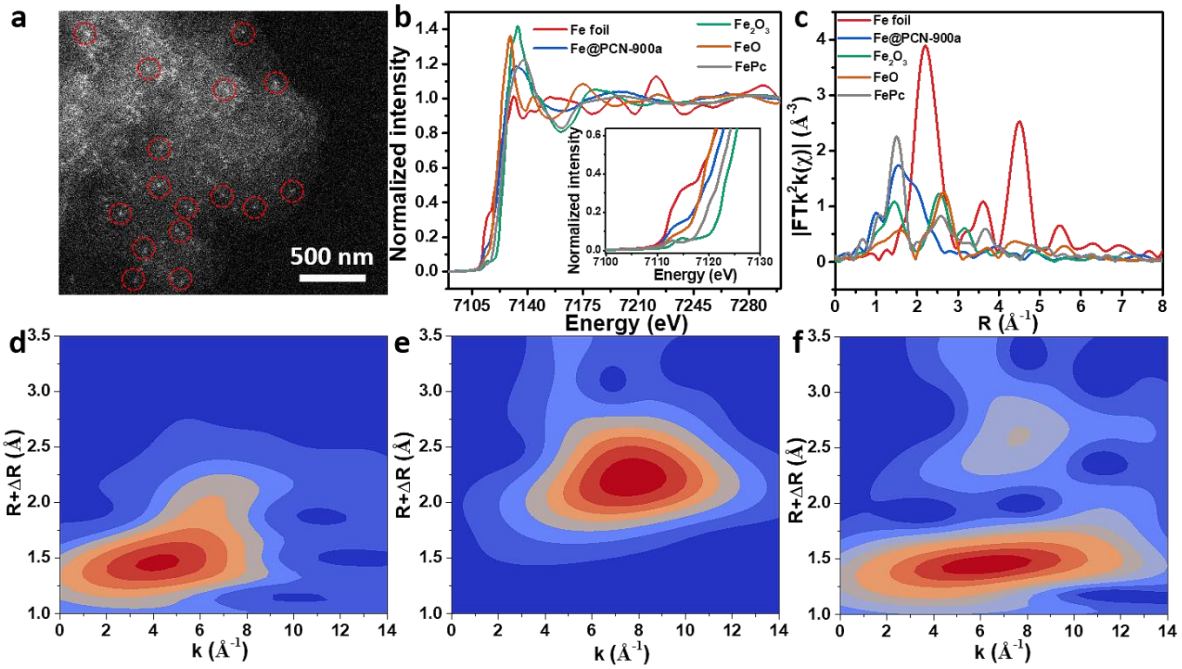


**Fig. 2.** The single-dispersed Fe characterization in Fe@PCN-900a. **(**a) HAADF-STEM image of Fe@PCN-900a. (b) Normalized Fe K-edge XANES spectra and (c) EXAFS spectra of Fe@PCN-900a, FePc, Fe foil, FeO and $Fe_2O_3$. Wavelet transform of Fe K-edge EXAFS for (d) Fe@PCN-900a, (e) Fe foil and (f) FePc.

Because of the easily controlled 2D morphology and large specific surface areas after pyrolysis, GPAz can be used as an ideal supporter for loading transition metal elements. GPAz was dispersed in an aqueous solution of $FeCl_3$ to absorb $Fe^{3+}$ onto the polymer nanosheets. As-produced $Fe^{3+}$-anchored polymer nanosheets ($Fe^{3+}$@GPAz) were then pyrolyzed at 800–1000 °C in an Ar atmosphere for 2 h to produced Fe/N co-doped porous carbon nanosheets (Fe@PCN-T,

T = 800, 900, and 1000, Scheme 1). In order to activate the samples [49,50], Fe@PCN-T was further treated by $NH_3$ for 20 min to produce activated Fe/N co-doped porous carbon nanosheets (denoted as Fe@PCN-Ta, T = 800, 900, 1000). Control samples (Fe@PC-Ta and Fe@PCN'-Ta) were prepared using the same method based on $Fe^{3+}$-adbsorbed PAz and GPNA precursors. Typically, the TEM images of Fe@PCN-900a in Fig. S12 show a uniform sheet-like structure, indicating that the 2D morphology can be easily maintained after involving metal ions and activation processes. High-resolution TEM (HRTEM) images and electron diffraction in corresponding selected areas (Fig. S12i) demonstrate that Fe@PCN-900a partly graphitized. The bright spots in high-angle annular dark-field imaging scanning TEM (HAADF-STEM) images (Fig. 2a) reveal atomically dispersed Fe atoms on the as-prepared material. The elemental mapping images obtained from energy dispersive X-ray analysis exhibit homogeneous distribution of C, N, and Fe elements in Fe@PCN-900a (Fig. S13). From the XRD pattern of Fe@PCN-900a (Fig. S14a), no signature peaks of Fe species were found, suggesting Fe particles have been removed. The peaks at around 26° and 44° can be assigned to the (002) and (100) planes of graphitized carbon. The inductively coupled plasma optical result indicates that 1.44% of Fe remained in Fe@PCN-900a. As shown in Raman spectra (Fig. S14b), the $I_D/I_G$ value of Fe@PCN'-900a is 1.01, which is lower than the $I_D/I_G$ value of Fe@PCN-900a (1.07), indicating the defects in Fe@PCN-900a are at relatively high concentration. These atomic Fe-dispersed carbon nanosheets exhibit large specific surface area and Fe content, revealing its high potential in the field of electrocatalysis.

To study the atomic Fe coordination environment and chemical state, X-ray absorption near-edge structure (XANES) was performed. As shown in Fig. 2b, the XANES curve of Fe@PCN-900a shows a greater near-edge absorption energy than that of FeO but weaker than that of $Fe_2O_3$,

indicating that the valency of the Fe atom is situated between $Fe^{2+}$ and $Fe^{3+}$. A weak pre-edge peak at approximately 7114.5 eV is regarded as the fingerprint of the $FeN_4$ square-planar structure [51-53]. From the extended X-ray absorption fine structure (EXAFS) spectra (Fig. 2c), the peaks of Fe–Fe coordination (2.15 Å) were not observed, which is in agreement with the results of XRD patterns and HAADF-STEM images. Fe@PCN-900a demonstrates a peak at 1.50 Å, which can be assigned to Fe−N coordination [54]. Wavelet transform of Fe K-edge EXAFS further demonstrates the coordination environment of Fe in an intuitive way. As presented in Fig. 2d, the most intense signal of Fe@PCN-900a centered at (4.2 $Å^{-1}$, 1.5 Å), completely different from Fe foil (5.2 $Å^{-1}$, 2.6 Å) (Fig. 2e). In addition, such signal is close to iron phthalocyanine (FePc, Fig. 2f), indicating Fe@PCN-900a has a similar coordination environment of FePc. The C1s X-ray photoelectron spectroscopy (XPS, Fig. S15-16) results assigned the peaks of Fe@PCN-900a, Fe@PCN'-900a and Fe@PC-900a at 284.5, 284.9, and 285.5 eV to –C=C–, –C–C–, and –C–N–, respectively. The N1s XPS spectra can be divided into four peaks at 398.5, 399.4, 401.0, and 404.0 eV, corresponding to pyridinic-N, pyrrolic-N, graphitic-N, and oxidized-N, respectively. The content of pyridinic-N for Fe@PCN-900a (0.33 at.%) is higher than that of Fe@PC-900a (0.15 at.%) and Fe@PCN'-900a (0.11 at.%). Fig. S15c shows the high-resolution Fe 2p spectra, where the deconvolution yields two pairs of peaks for $Fe^{2+}$ (709.5 and 722.5 eV) and $Fe^{3+}$ (712.2 and 725.3 eV), and a satellite peak at 718.3 eV, indicating the co-existence of Fe(II) and Fe(III) in the catalysts, consistent with the results of XANES. The binding energy of Fe 2p at 711 eV implies the possible existence of $FeN_x$ species [55,56]. Because of the abundance of N elements and azulene units, the GPAz nanosheets can easily absorb metal atoms to form stable coordination structures before aggregation. This strategy could be a general method to fabricate single-metal-atom-dispersed carbon nanosheets.

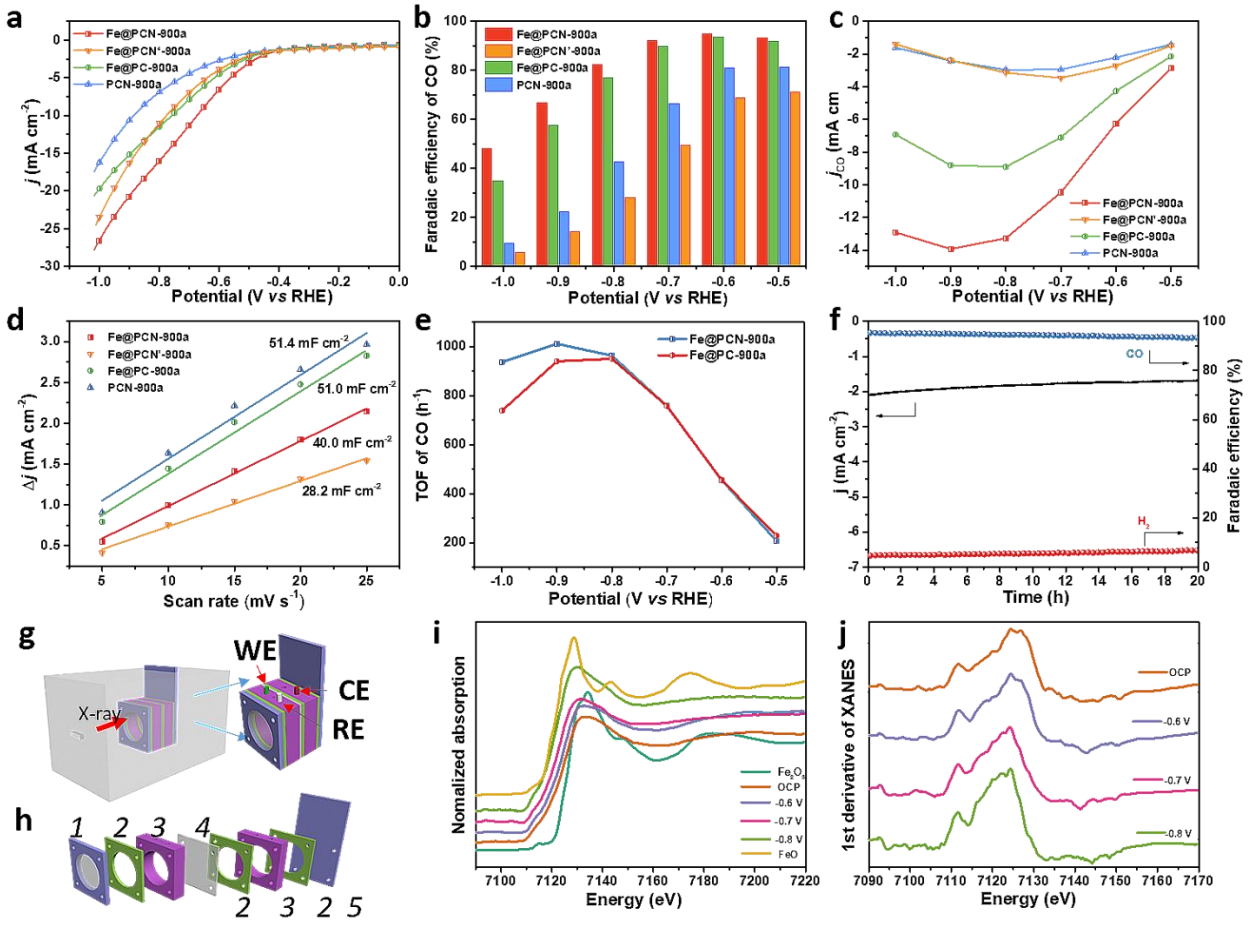


**Fig. 3.** Electrochemical evaluation and operando X-ray absorption spectroscopy. (a) LSV curves, (b) $FE_{CO}$, (c) CO partial current densities and (d) Capacitive current at 0.75 V as a function of scan rate for Fe@PCN-900a, Fe@PCN'-900a, PCN-900, and Fe@PC-900a in $CO_2$-saturated 0.5 M $KHCO_3$. (e) TOF values of Fe@PCN-900a and Fe@PC-900a at different potentials. (f) Stability test for Fe@PCN-900a. (g) Cartoon diagram of the device for operando XANES study of $CO_2$RRs (WE: working electrode; CE: counter electrode; RE: reference electrode). (h) Disassembled device for $CO_2$RRs (1: stain steel; 2: silicone gasket; 3: anode and cathode tank; 4: membrane; 5: stain steel). (i) Operando Fe K-edge XANES spectra and (j) the first derivative of the spectra of Fe@PCN-900a under different operating voltages.

Benefiting from the high specific surface and atomically dispersed Fe atoms, the as-prepared materials were used as catalysts for $CO_2$RR. To evaluate the $CO_2$RR activity of as-prepared materials, linear sweep voltammetry (LSV) was performed in $CO_2$-saturated 0.5 M $KHCO_3$ solution (Fig. 3a). Fe@PCN-900a exhibits a much higher total current density than that of Fe@PCN'-900a, Fe@PC-900a and PCN-900a from −0.5 to −1.0 V. The onset potentials for Fe@PCN-900a, Fe@PCN'-900a, Fe@PC-900a, and PCN-900a are −0.41 V, −0.49 V −0.46 V, −0.53 V, respectively. Comparing the LSV curves of Fe@PCN-900a in $CO_2$- and Ar-saturated 0.5 M $KHCO_3$ solutions (Fig. S17), a much higher current density and lower onset potential are observed in the $CO_2$-saturated solution, indicating Fe@PCN-900a has higher activity for $CO_2$RR. Gas chromatography and $^1$H nuclear magnetic resonance ($^1$H NMR) spectroscopy were then used to analyze the products of $CO_2$RR. The results reveal that CO is the dominant product and no liquid products are generated from $CO_2$RR (Fig. S18). Among all these catalysts, Fe@PCN-900a exhibits the highest selectivity for CO production with a maximum CO Faraday efficiency ($FE_{CO}$) of 95.3% at −0.6 V (vs. RHE). The maximum $FE_{CO}$ of Fe@PCN'-900a Fe@PC-900a and PCN-900a reached 71.4%, 94.0% and 81.2%, respectively (Fig. 3b). The CO partial current density of Fe@PCN-900a is much higher than that of Fe@PC-900a and PCN-900a (Fig. 3c). At −0.9 V, Fe@PCN-900a achieves a current density of 13.9 mA $cm^{-2}$, which is respectively 5.8, 1.6 and 5.8 times higher than that of Fe@PCN'-900a, Fe@PC-900a and PCN-900a, indicating that the $CO_2$RR activity trend is Fe@PCN-900a > Fe@PC-900a > Fe@PCN'-900a = PCN-900a. The high catalytic activity of Fe@PCN-900a mainly originate from the synergistic effects of topological defects and Fe-$N_4$ site. Then, CV measurements were performed at different scan rates (varying from 5 to 30 $mVs^{-1}$) to assess the effective surface area (Fig. 3d and Fig. S19). After calculation, the double-layer capacitances of Fe@PCN-900a, Fe@PC-900a, and PCN-900a are 40.0, 50.0, and 51.4 mF

$cm^{-2}$, respectively, indicating that PCN-900a displays the largest active surface area. Although Fe@PCN-900a exhibits smaller active surface area than PCN-900 and Fe@PC-900a, its performance remains the best. As shown in Fig. 3e, the turnover frequency (TOF) of Fe@PCN-900a reaches 1011 $h^{-1}$ at the potential of 0.9 V, higher than that of Fe@PC-900a (940 $h^{-1}$), indicating that Fe@PCN-900a has a higher intrinsic catalyst efficiency than Fe@PC-900a. Fe@PCN-900a shows the lowest Tafel slope of 310 mV $dec^{-1}$ among the catalysts, implying the fastest kinetics for the CO formation (Fig. S20). The stability of Fe@PCN-900a was tested at a constant potential of −0.6 V (vs. RHE). After 20 h test, The $FE_{CO}$ of Fe@PCN-900a decreases from 95.3 % to 93.4 %, maintaining 98% of its original performance (Fig. 3f), while $FE_{CO}$ of Fe@PCN'-900a decreased 4.1% after stability test (Fig. S21). Other than high electrocatalytic activity and selectivity, Fe@PCN-900a also exhibited high long-term stability. Besides, the valency of the Fe atom scarcely changed after long-time test from normalized Fe K-edge XANES spectrum of Fe@PCN-900a after stability test (Fig. S22). Other results during the performance optimization process are shown in Fig. S23-25. High activity and selectivity as well as adequate stability make Fe@PCN-900a a promising candidate for $CO_2$RR.

Operando XANES measurements were performed to further clarify the relationship between the catalytic activity and valence state of the Fe element during the $CO_2$RR process. The schematic of the $CO_2$RR operando XANES device and detailed illustration of a $CO_2$RR electrolytic cell are shown in Fig. S3g and 3h. Operando XANES measurements were conducted under open-circuit potential (OCP, −0.2 V), −0.6 V, −0.7 V and −0.8 V (vs RHE), respectively. From the Fe K-edge XANES spectra (Fig. 3i), the absorption edge of Fe@PCN-900a at −0.6 V shows a slight shift to lower energies from Fe@PCN-900a at OCP. After increasing the potential, the Fe K-edge shifted to lower energies more clearly, indicating the reduction of $Fe^{3+}$ to $Fe^{2+}$. This trend is consistent

with that of the $FE_{CO}$ of Fe@PCN-900a at different potentials. Fe@PCN-900a shows the highest $FE_{CO}$ at −0.6 V. After increasing the potential to −0.8 V, the $FE_{CO}$ sharply declines from 95.3% to 82.6%. From the first derivative of XANES spectra (Fig. 3j), the shift to lower energies from OCP to −0.8 V can be more clearly observed. Operando XANES characterization indicates that $Fe^{3+}$ is a significant active center for $CO_2RR$. After reducing to $Fe^{2+}$, the activity and selectivity of the catalyst decreases.

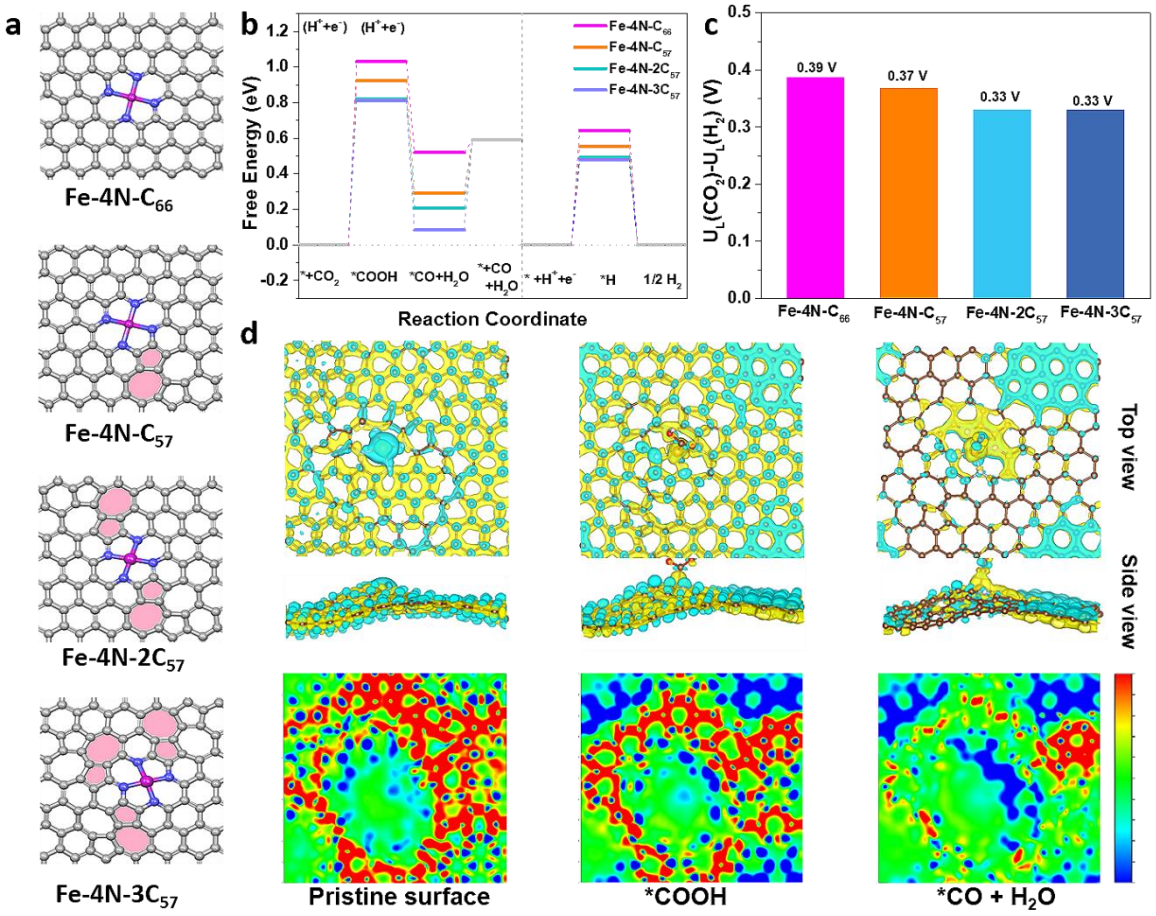


**Fig. 4.** DFT studies. (a) The representative models for DFT calculations: Fe-4N-$C_{66}$, Fe-4N-$C_{57}$, Fe-4N-$2C_{57}$ and Fe-4N-$3C_{57}$. (b) Free energy diagrams for different models. (c) The differences in limiting potentials for $CO_2RR$ ($U_L(CO_2)$) and HER ($U_L(H_2)$) over different models. (d) Charge

density difference of reaction transition state of Fe-4N-3$C_{57}$ (top: top view, middle: side view, bottom: 2D slice).

DFT simulation was performed to investigate the relationship between superior performance and the structure of as-prepared electrocatalysts. For studying the influence of $C_{57}$ defects (five-carbon-ring-adjacent to seven-carbon ring) on the activity of the catalysts, four carbon models were built (Fig. 4a), including Fe-4N-$C_{66}$, Fe-4N-$C_{57}$, Fe-4N-2$C_{57}$, and Fe-4N-3$C_{57}$, with increasing $C_{57}$ defects in the carbon skeleton. The detailed optimization process and calculated data are shown in Fig. S26-39 and Table S2-S3. Fe-4N-$C_{57}$ was used as a typical example to illustrate the mechanism during $CO_2$ reduction process (Fig. S39). The electrochemical reduction of $CO_2$ to CO involves two proton/electron transfer steps. $CO_2$ is first adsorbed on the Fe-$N_4$ sites, accompanying with a proton and an electron to generate COOH* ($CO_2$+*+$H^+$+$e^-$→*COOH). Then, COOH* further hydrogenates to form CO* (*COOH+$H^+$+$e^-$→*CO+$H_2O$). Finally, *CO desorb from the catalyst surface to form CO. Generally, *COOH formation step exhibits a large energy barrier and is considered as the rate-determining step. From the free energy diagrams of $CO_2$ reduction of four types of active sites (Fig. 4b), Fe-4N-$C_{66}$, which has no $C_{57}$ defects in the carbon skeleton, exhibits the largest energy barrier of 1.03 eV at the first step. When the number of $C_{57}$ defects increases, the energy barrier declines. Fe-4N-3$C_{57}$ with three $C_{57}$ defects shows the lowest energy barrier of 0.81 eV. This result indicates that $C_{57}$ defects can effectively decrease the energy barrier of $CO_2$ transition to COOH*. Compared with other $FeN_x$ models without topological defects reported in the literature (Table S4), Fe-4N-3$C_{57}$ shows a lower energy barrier than most of the models [57-60]. Free energy diagrams of each active site during HER process are also shown in Fig. 4b. Fe-4N-$C_{66}$ exhibits the highest energy barrier of 0.64 eV. The energy barrier declines as the number of $C_{57}$ defects increases. Furthermore, the $CO_2$ reduction selectivity has

been taken into account by calculating the difference in limiting potentials of $CO_2$RR and HER ($U_L(CO_2)$-$U_L(H_2)$) of different models. As shown in Fig. 4c, Fe-4N-3$C_{57}$ and Fe-4N-2$C_{57}$ show the lowest value of $U_L(CO_2)$-$U_L(H_2)$, suggesting the highest selectivity for $CO_2$RR. Charge density difference can provide clear information for illustrating the interaction at the interface. As shown in Fig. 4d, yellow and cyan represent charge accumulation and depletion in the region. For a pristine surface, the charge accumulation occurs around the $C_{57}$ defect, whereas the charge depletes at the $FeN_4$ site. Charge redistribution takes place when a $CO_2$ molecule is adsorbed. Charge accumulates on the interface between the *COOH and $FeN_4$ sites, leading to the generation of highly active regions for the electrocatalytic process. Next, *COOH gets one electron to form *CO and the charge further accumulates on the interface. The 2D slice pictures exhibit a higher charge density around the $C_{57}$-defect-enriched carbon. As the reaction proceeds, the charge density gradually decreases. The result indicated that the electrons tend to transfer from the $C_{57}$-defect-enriched carbon to the $FeN_4$ site, and eventually, to $CO_2$. Therefore, topological defects involving single-Fe-dispersed active sites not only can effectively decrease the energy barrier but also increase the CO selectivity during $CO_2$RR process, rendering Fe@PCN-900a exhibits high Faradaic efficiency of CO.

**4. Conclusion**

In conclusion, atomically dispersed porous carbon nanosheets were rationally synthesized using azulene-based material as precursor. The as-prepared elecrocatalysts displayed a uniform 2D structure, large specific surface area, and high density of active sites, which are all beneficial for promising CO2RR performance. Operando XANES and DFT analyses revealed that topological defects involving single Fe active sites can effectively decrease the energy barrier for

$CO_2$RR. This study thus demonstrated a novel method of designing and preparing SACs with rich topological defects in large quantity for a remarkable performance of electrocatalysis.

**Conflicts of interest**

The authors declare no conflicts of interest.

**Acknowledgements**

J. Ding and D. Wu contributed equally to this work. The authors are grateful for the financial support from the National Key R&D Program of China (2017YFB0405600, 2017YFE9134000), the NSFC (51973114, 21720102002, 51811530013). Y. Chen thanks the support from National Natural Science Foundation of China (51333002, 61674153, 61722407, 51973061, 61974090), the Natural Science Foundation of Shanghai (19JC412600, 19ZR1413100 and 19ZR1474500), and the Fundamental Research Funds for the Central Universities (50321041918013). J. Zhang is grateful for the support from NSFC (11705270, 11975100). The authors thank the support from Instrumental Analysis Center and Center for High Performance Computing at Shanghai Jiao Tong University.

**Supporting Information**

The Supporting Information is available free of charge.

## References


[1] R.G. Mariano, K. McKelvey, H.S. White, M.W. Kanan, Selective increase in $CO_2$ electroreduction activity at grain-boundary surface terminations, Science 358 (2017) 1187−1192.

[2] S. Ren, D. Joulié, D. Salvatore, K. Torbensen, M. Wang, M. Robert, C.P. Berlinguette, Molecular electrocatalysts can mediate fast, selective $CO_2$ reduction in a flow cell, Science 365 (2019) 367−369.

[3] M.B. Ross, P. De Luna, Y. Li, C.T. Dinh, D. Kim, P. Yang, E.H. Sargent, Designing materials for electrochemical carbon dioxide recycling, Nat. Catal. 2 (2019) 648−658.

[4] R. Francke, B. Schille, M. Roemelt, Homogeneously catalyzed electroreduction of carbon dioxide-methods, mechanisms, and catalysts, Chem. Rev. 118 (2018) 4631−4701.

[5] T. Zheng, K. Jiang, H. Wang, Recent advances in electrochemical $CO_2$-to-CO conversion on heterogeneous catalysts, Adv. Mater. 30 (2018) 1802066.

[6] C.A. Trickett, A. Helal, B.A. Al-Maythalony, Z.H. Yamani, K.E. Cordova, O.M. Yaghi, The chemistry of metal-organic frameworks for $CO_2$ capture, regeneration and conversion, Nat. Rev. Mater. 2 (2017) 17045.

[7] H.B. Yang, S.F. Hung, S. Liu, K. Yuan, S. Miao, L. Zhang, X. Huang, H.Y. Wang, W. Cai, R. Chen, J. Gao, X. Yang, W. Chen, Y. Huang, H.M. Chen, C.M. Li, T. Zhang, B. Liu, Atomically dispersed Ni(I) as the active site for electrochemical $CO_2$ reduction, Nat. Energy 3 (2018) 140−147.

[8] C. Lu, J. Yang, S. Wei, S. Bi, Y. Xia, M. Chen, Y. Hou, M. Qiu, C. Yuan, Y. Su, F. Zhang, H. Liang, X. Zhuang, Atomic Ni anchored covalent triazine framework as high efficient electrocatalyst for carbon dioxide conversion, Adv. Funct. Mater. 29 (2019) 1806884.

[9] H. Mistry, Y.W. Choi, A. Bagger, F. Scholten, C.S. Bonifacio, I. Sinev, N.J. Divins, I. Zegkinoglou, H.S. Jeon, K. Kisslinger, E.A. Stach, J.C. Yang, J. Rossmeisl, B. Roldan Cuenya, Enhanced carbon dioxide electroreduction to carbon monoxide over defect-rich plasma-activated silver catalysts, Angew. Chem. Int. Ed. 129 (2017) 11552−11556.

[10] S. Nitopi, E. Bertheussen, S.B. Scott, X. Liu, A.K. Engstfeld, S. Horch, B. Seger, I.E.L. Stephens, K. Chan, C. Hahn, J.K. Norskov, T.F. Jaramillo, I. Chorkendorff, Progress and perspectives of electrochemical $CO_2$ reduction on copper in aqueous electrolyte, Chem. Rev. 119 (2019) 7610−7672.

[11] A.S. Varela, W. Ju, P. Strasser, Molecular nitrogen–carbon catalysts, solid metal organic framework catalysts, and solid metal/nitrogen-doped carbon (MNC) catalysts for the electrochemical $CO_2$ reduction, Adv. Energy Mater. 8 (2018) 1703614.

[12] C. Cometto, L. Chen, P.K. Lo, Z. Guo, K.C. Lau, E. Anxolabehere-Mallart, C. Fave, T.C. Lau, M. Robert, Highly selective molecular catalysts for the $CO_2$-to-CO electrochemical conversion at very low overpotential. Contrasting Fe vs Co quaterpyridine complexes upon mechanistic studies, ACS Catal. 8 (2018) 3411−3417.

[13] J. Gu, C.S. Hsu, L. Bai, H.M. Chen, X. Hu, Atomically dispersed $Fe^{(3+)}$ sites catalyze efficient $CO_2$ electroreduction to CO, Science 364 (2019) 1091−1094.

[14] Y. Pan, R. Lin, Y. Chen, S. Liu, W. Zhu, X. Cao, W. Chen, K. Wu, W.C. Cheong, Y. Wang, L. Zheng, J. Luo, Y. Lin, Y. Liu, C. Liu, J. Li, Q. Lu, X. Chen, D. Wang, Q. Peng, C. Chen, Y. Li, Design of single-atom Co-$N_5$ catalytic site: a robust electrocatalyst for $CO_2$ reduction with nearly 100% CO selectivity and remarkable stability, J. Am. Chem. Soc. 140 (2018) 4218−4221.

[15] Y. Cheng, S. Zhao, B. Johannessen, J.P. Veder, M. Saunders, M.R. Rowles, M. Cheng, C. Liu, M.F. Chisholm, R. De Marco, H.M. Cheng, S.Z. Yang, S.P. Jiang, Atomically dispersed transition metals on carbon nanotubes with ultrahigh loading for selective electrochemical carbon dioxide reduction, Adv. Mater. 30 (2018) 1706287.

[16] S. Ji, Y. Chen, X. Wang, Z. Zhang, D. Wang, Y. Li, Chemical synthesis of single atomic site catalysts, Chem. Rev. 120 (2020) 11900−11955.

[17] Z. Lei, Y. Xue, W. Chen, W. Qiu, Y. Zhang, S. Horike, L. Tang, MOFs-based heterogeneous catalysts: new opportunities for energy-related $CO_2$ conversion, Adv. Energy Mater. 8 (2018) 1801587.

[18] C.E. Tornow, M.R. Thorson, S. Ma, A.A. Gewirth, P.J.A. Kenis, Nitrogen-based catalysts for the electrochemical reduction of $CO_2$ to CO, J. Am. Chem. Soc. 134 (2012) 19520−19523.

[19] X. Xue, H. Yang, T. Yang, P. Yuan, Q. Li, S. Mu, X. Zheng, L. Chi, J. Zhu, Y. Li, J. Zhang, Q. Xu, N,P-coordinated fullerene-like carbon nanostructures with dual active centers toward highly-efficient multi-functional electrocatalysis for $CO_2$RR, ORR and Zn-air battery, J. Mater. Chem. A 7 (2019) 15271−15277.

[20] P.P. Sharma, J. Wu, R.M. Yadav, M. Liu, C.J. Wright, C.S. Tiwary, B.I. Yakobson, J. Lou, P.M. Ajayan, X.D. Zhou, Nitrogen-doped carbon nanotube arrays for high-efficiency electrochemical reduction of $CO_2$: on the understanding of defects, defect density, and selectivity, Angew. Chem. Int. Ed. 54 (2015) 13701−13705.

[21] X. Zou, M. Liu, J. Wu, P.M. Ajayan, J. Li, B. Liu, B.I. Yakobson, How nitrogen-doped graphene quantum dots catalyze electroreduction of $CO_2$ to hydrocarbons and oxygenates, ACS Catal. 7 (2017) 6245−6250.

[22] E. Li, F. Yang, Z. Wu, Y. Wang, M. Ruan, P. Song, W. Xing, W. Xu, A bifunctional highly efficient FeNx/C electrocatalyst, Small 14 (2018) 1702827.

[23] H. Zhang, J. Li, S. Xi, Y. Du, X. Hai, J. Wang, H. Xu, G. Wu, J. Zhang, J. Lu, J. Wang, A graphene supported single-atom $FeN_5$ catalytic site for efficient electrochemical $CO_2$ reduction, Angew. Chem. Int. Ed. 58 (2019) 14871−14876.

[24] C. Zhang, S. Yang, J. Wu, M. Liu, S. Yazdi, M. Ren, J. Sha, J. Zhong, K. Nie, A.S. Jalilov, Z. Li, H. Li, B.I. Yakobson, Q. Wu, E. Ringe, H. Xu, P.M. Ajayan, J.M. Tour, Electrochemical $CO_2$ reduction with atomic iron-dispersed on nitrogen-doped graphene, Adv. Energy Mater., 2018, 8, 1703487.

[25] Y. Wang, J. Mao, X. Meng, L. Yu, D. Deng, X. Bao, Catalysis with two-dimensional materials confining single atoms: concept, design, and applications, Chem. Rev. 119 (2019) 1806−1854.

[26] Y. Cheng, J. Zhang, X. Wu, C. Tang, S. Yang, P. Su, L. Thomsen, F. Zhao, S. Lu, J. Liu, S.P. Jiang, A template-free method to synthesis high density iron single atoms anchored on carbon nanotubes for high temperature polymer electrolyte membrane fuel cells, Nano Energy, 80 (2021) 105534.

[27] P. Su, W. Huang, J. Zhang, U. Guharoy, Q. Du, Q. Sun, Q. Jiang, Y. Cheng, J. Yang, X. Zhang, Y. Liu, S.P. Jiang, J. Liu, Fe atoms anchored on defective nitrogen doped hollow carbon spheres as efficient electrocatalysts for oxygen reduction reaction, Nano Res., 14 (2021) 1069−1077.

[28] X. Wang, S. Qiu, J. Feng, Y. Tong, F. Zhou, Q. Li, L. Song, S. Chen, K.-H. Wu, P. Su, S. Ye, F. Hou, S.X. Dou, H.K. Liu, G.Q. Lu, C. Sun, J. Liu, J. Liang, Confined Fe–Cu Clusters as

Sub-Nanometer Reactors for Efficiently Regulating the Electrochemical Nitrogen Reduction Reaction, Adv. Mater., 32 (2020) 2004382.

[29] Y. Wang, Z. Li, P. Zhang, Y. Pan, Y. Zhang, Q. Cai, S.R.P. Silva, J. Liu, G. Zhang, X. Sun, Z. Yan, Flexible carbon nanofiber film with diatomic Fe-Co sites for efficient oxygen reduction and evolution reactions in wearable zinc-air batteries, Nano Energy, 87 (2021) 106147.

[30] Z. Zhang, Y. Chen, L. Zhou, C. Chen, Z. Han, B. Zhang, Q. Wu, L. Yang, L. Du, Y. Bu, P. Wang, X. Wang, H. Yang, Z. Hu, The simplest construction of single-site catalysts by the synergism of micropore trapping and nitrogen anchoring, Nat. Commun. 10 (2019) 1657.

[31] Y. Xue, B. Huang, Y. Yi, Y. Guo, Z. Zuo, Y. Li, Z. Jia, H. Liu, Y. Li, Anchoring zero valence single atoms of nickel and iron on graphdiyne for hydrogen evolution, Nat. Commun. 9 (2018) 1460.

[32] L. Dai, Y. Xue, L. Qu, H.J. Choi, J.B. Baek, Metal-free catalysts for oxygen reduction reaction, Chem. Rev. 115 (2015) 4823−4892.

[33] A.V. Krasheninnikov, F. Banhart, Engineering of nanostructured carbon materials with electron or ion beams, Nat. Mater. 6 (2007) 723−733.

[34] A.V. Krasheninnikov, K. Nordlund, Ion and electron irradiation-induced effects in nanostructured materials, J. Appl. Phys. 107 (2010) 071301.

[35] X. Yan, Y. Jia, X. Yao, Defects on carbons for electrocatalytic oxygen reduction, Chem. Soc. Rev. 47 (2018) 7628−7658.

[36] L. Wang, W. Chen, D. Zhang, Y. Du, R. Amal, S. Qiao, J. Wu, Z. Yin, Surface strategies for catalytic $CO_2$ reduction: from two-dimensional materials to nanoclusters to single atoms, Chem. Soc. Rev. 48 (2019) 5310−5349.

[37] Y. Wang, P. Han, X. Lv, L. Zhang, G. Zheng, Defect and interface engineering for aqueous electrocatalytic $CO_2$ reduction, Joule 2 (2018) 2551−2582.

[38] W. Wang, L. Shang, G. Chang, C. Yan, R. Shi, Y. Zhao, G.I.N. Waterhouse, D. Yang, T. Zhang, Intrinsic carbon-defect-driven electrocatalytic reduction of carbon dioxide, Adv. Mater. 31 (2019) 1808276.

[39] S. Siahrostami, K. Jiang, M. Karamad, K. Chan, H. Wang, J. Nørskov, Theoretical investigations into defected graphene for electrochemical reduction of $CO_2$, ACS Sustain. Chem. Eng. 5 (2017) 11080−11085.

[40] Y. Jia, K. Jiang, H. Wang, X. Yao, The role of defect sites in nanomaterials for electrocatalytic energy conversion, Chem 5 (2019) 1371−1397.

[41] J. Lin, Z. Peng, Y. Liu, F. Ruiz-Zepeda, R. Ye, E.L.G. Samuel, M.J. Yacaman, B.I. Yakobson, J.M. Tour, Laser-induced porous graphene films from commercial polymers, Nat. Commun. 5 (2014) 5714.

[42] Q.H. Wang, M.S. Strano, Carbon nanotubes: a bright future for defects, Nat. Chem. 5 (2013) 812−813.

[43] T. Humberto, L. Ruitao, T. Mauricio, S.D. Mildred, The role of defects and doping in 2D graphene sheets and 1D nanoribbons, Rep. Prog. Phys. 75 (2012) 062501.

[44] B. Feng, X. Zhuang, The philosophy of carbon: meso-entropy materials, Faraday Discuss. 227 (2020) 80−90.

[45] B. Feng, X. Zhuang, Carbon-Enriched meso-Entropy Materials: from Theory to Cases, Acta Chim. Sinica, 78 (2020) 833-847

[46] T. Zhang, Y. Hou, V. Dzhagan, Z. Liao, G. Chai, M. Loffler, D. Olianas, A. Milani, S. Xu, M. Tommasini, D.R.T. Zahn, Z. Zheng, E. Zschech, R. Jordan, X. Feng, Copper-surface-

mediated synthesis of acetylenic carbon-rich nanofibers for active metal-free photocathodes, Nat. Commun. 9 (2018) 1140.

[47] M. Murai, E. Amir, R.J. Amir, C.J. Hawker, Azulene-based conjugated polymers: unique seven-membered ring connectivity leading to stimuli-responsiveness, Chem. Sci. 3 (2012) 2721−2725.

[48] F. Gerson, M. Scholz, H.J. Hansen, P. Uebelhart, Radical cations of alkylazulenes - an EPR and ENDOR study, J. Chem. Soc. Perk. T. 2, 2 (1995) 215−220.

[49] Y. Dong, Q. Zhang, Z. Tian, B. Li, W. Yan, S. Wang, K. Jiang, J. Su, C. W. Oloman, E.L. Gyenge, R. Ge, Z. Lu, X. Ji, L. Chen, Ammonia thermal treatment toward topological defects in porous carbon for enhanced carbon dioxide electroreduction, Adv. Mater. 32 (2020) 2001300.

[50] J. Zhu, Y. Huang, W. Mei, C. Zhao, C. Zhang, J. Zhang, I.S. Amiinu, S. Mu, Effects of intrinsic pentagon defects on electrochemical reactivity of carbon nanomaterials, Angew. Chem. Int. Ed. 131 (2019) 3899−3904.

[51] K. Yuan, S. Sfaelou, M. Qiu, D. Lützenkirchen-Hecht, X. Zhuang, Y. Chen, C. Yuan, X. Feng, U. Scherf, Synergetic contribution of boron and Fe–Nx species in porous carbons toward efficient electrocatalysts for oxygen reduction reaction, ACS Energy Lett. 3 (2018) 252−260.

[52] Q.L. Zhu, W. Xia, L.R. Zheng, R. Zou, Z. Liu, Q. Xu, Atomically dispersed Fe/N-doped hierarchical carbon architectures derived from a metal–organic framework composite for extremely efficient electrocatalysis, ACS Energy Lett., 2 (2017) 504−511.

[53] Q. Liu, X. Liu, L. Zheng, J. Shui, The solid-phase synthesis of an Fe-N-C electrocatalyst for high-power proton-exchange membrane fuel cells, Angew. Chem. Int. Ed. 57 (2018) 1204−1208.

[54] W. Liu, L. Zhang, X. Liu, X. Liu, X. Yang, S. Miao, W. Wang, A. Wang, T. Zhang, Discriminating catalytically active FeNx species of atomically dispersed Fe-N-C catalyst for selective oxidation of the C-H bond, J. Am. Chem. Soc. 139 (2017) 10790−10798.

[55] Y. Wang, A. Kong, X. Chen, Q. Lin, P. Feng, Efficient oxygen electroreduction: hierarchical porous Fe–N-doped hollow carbon nanoshells, ACS Catal. 5 (2015) 3887−3893.

[56] Y. Ding, Y. Niu, J. Yang, L. Ma, J. Liu, Y. Xiong, H. Xu, A metal-amino acid complex-derived bifunctional oxygen electrocatalyst for rechargeable zinc-air batteries, Small 12 (2016) 5414−5421.

[57] Q. Cheng, K. Mao, L. Ma, L. Yang, L. Zou, Z. Zou, Z. Hu, H. Yang, Encapsulation of iron nitride by Fe-N-C shell enabling highly efficient electroreduction of $CO_2$ to CO, ACS Energy Lett. 3 (2018) 1205−1211.

[58] F. Pan, H. Zhang, K. Liu, D. Cullen, K. More, M. Wang, Z. Feng, G. Wang, G. Wu, Y. Li, Unveiling active sites of $CO_2$ reduction on nitrogen-coordinated and atomically dispersed iron and cobalt catalysts, ACS Catal. 8 (2018) 3116−3122.

[59] X. Qin, S. Zhu, F. Xiao, L. Zhang, M. Shao, Active sites on heterogeneous single-iron-atom electrocatalysts in $CO_2$ reduction reaction, ACS Energy Lett. 4 (2019) 1778−1783.

[60] Y. Wang, M. Wang, Z. Zhang, Q. Wang, Z. Jiang, M. Lucero, X. Zhang, X. Li, M. Gu, Z. Feng, Y. Liang, Phthalocyanine precursors to construct atomically dispersed iron electrocatalysts, ACS Catal. 9 (2019) 6252−6261.